# A multi-wavelength optoelectronic synapse with 2D materials for mixed-color pattern recognition

Molla Manjurul Islam,<sup>1, 2</sup> Adithi Krishnaprasad,<sup>1, 3</sup> Durjoy Dev,<sup>1, 3</sup> Ricardo Martinez-Martinez,<sup>1, 3</sup> Victor Okonkwo,<sup>1</sup> Benjamin Wu,<sup>5</sup> Sang Sub Han,<sup>1</sup> Tae-Sung Bae,<sup>7</sup> Hee-Suk Chung,<sup>7</sup> Jimmy Touma,<sup>6</sup> Yeonwoong Jung<sup>1, 3, 4</sup> and Tania Roy<sup>1, 2, 3, 4, \*</sup>

<sup>1</sup>NanoScience Technology Center, University of Central Florida, Orlando, FL 32826, USA

<sup>2</sup>Department of Physics, University of Central Florida, Orlando, FL 32816, USA

<sup>3</sup>Department of Electrical and Computer Engineering, University of Central Florida, Orlando, FL 32816, USA

<sup>4</sup>Department of Materials Science and Engineering, University of Central Florida, Orlando, FL 32816, USA

<sup>5</sup>Department of Applied Mathematics and Statistics, Stony Brook University, Stony Brook, NY 11794, USA

<sup>6</sup>Air Force Research Lab, Eglin Air Force Base, FL 32542, USA

<sup>7</sup>Analytical Research Division, Korea Basic Science Institute, Jeonju 54907, South Korea

\*Corresponding author: tania.roy@ucf.edu

#### **ABSTRACT**

Neuromorphic visual systems emulating biological retina functionalities have enormous potential for in-sensor computing, with prospects of making artificial intelligence ubiquitous. Conventionally, visual information is captured by an image sensor, stored by memory units, and eventually processed by the machine learning algorithm. Here we present an optoelectronic synapse device with multifunctional integration of all the processes required for real time object identification. Ultraviolet-visible wavelength-sensitive MoS<sub>2</sub> FET channel with infrared sensitive PtTe<sub>2</sub>/Si gate electrode enables the device to sense, store, and process optical data for a wide range of the electromagnetic spectrum, while maintaining a low dark current. The device exhibits optical stimulation-controlled short term and long term potentiation, electrically driven long term depression, synaptic weight update for multiple wavelengths of light ranging from 300 nm in ultraviolet to 2 µm in infrared. An artificial neural network developed using the extracted weight update parameters of the device can be trained to identify both single wavelength and mixed wavelength patterns. This work demonstrates a device that could potentially be used for realizing of a multi-wavelength neuromorphic visual system for pattern recognition and object identification.

KEYWORDS: optoelectronic synapse, multi-wavelength, monolayer MoS<sub>2</sub>, PtTe<sub>2</sub>, neuromorphic device, nonvolatile, phototransistor.

#### INTRODUCTION

The rapidly evolving artificial visual systems demand an enormous amount of optical data sensing and real time processing to be deployed in object identification.<sup>1,2</sup> Conventional artificial

visual systems include separate image sensors to perceive the visual information, memory blocks to store the data and processing units for pattern recognition and object identification. These systems produce an abundance of data requiring complex computation to discard redundant data and extract significant information.<sup>3</sup> This complex computation is performed by uploading the datasets to the cloud and applying machine learning algorithms for processing, which results in system latency and enormous power consumption.<sup>4, 5</sup> Although neuromorphic systems with artificial neurons and synapses can create a neural network to overcome this bottleneck, they still require image sensors and bulky circuitry to convert the image into electrical signals.<sup>1, 6</sup> However, like the sensory neurons in the human eye, an optoelectronic synapse can directly sense the optical data and store it through conductance states, which enables it to perform optical data sensing, storage, and processing in the same device. 1, 2, 7 Because of these potential advantages of optoelectronic synapses, many sophisticated devices have been realized using 1D carbon nano tube (CNT),<sup>8, 9</sup> 2D MoS<sub>2</sub>,<sup>5, 10-20</sup> black phosphorus,<sup>21</sup> graphene,<sup>22</sup> graphene oxides (GOs),<sup>23</sup> metal oxides, <sup>24-29</sup> organics, <sup>30</sup> and halide perovskites. <sup>31</sup> While photosensitivity of 2D materials is utilized to sense the optical data, material properties such as persistent photoconductivity or interface defects and techniques like floating gate engineering have been employed for charge trapping to execute optoelectronic synapse operations. Optically tuned conductance states in carbon nanotube transistors with poly(3-octylthiophene-2,5-diyl) (P3OT)-coating has been illustrated.<sup>8</sup> A device with a hybrid film of graphene and atomically thin single-walled carbon nanotubes (SWNTs) was demonstrated. <sup>22</sup> All optoelectronic synapse characteristics were mimicked using a layered 2D perovskite material sandwiched between top and bottom graphene layers,<sup>32</sup> while optoelectronic synaptic characteristics were also obtained by using a a single layer graphene as the channel material with methylammonium lead bromide perovskite quantum dots grown directly on top of the channel.<sup>33</sup> An optical synapse device based on few layers of black phosphorus (BP) was demonstrated.<sup>21</sup> A MoS<sub>2</sub>/p-Si heterostructure, and elsewhere multilayer MoS<sub>2</sub> with high-k Ta<sub>2</sub>O<sub>5</sub>-TiO<sub>2</sub> (TTO) is used to emulate optoelectronic synapse characteristics.<sup>5, 21</sup> An amorphous oxide semiconductor heterostructure with indium zinc oxide (IZO) and indium gallium zinc oxide (IGZO) was used to demonstrate optoelectronic synapse characteristics.<sup>34</sup> The hybrid structure of CsPb(Br<sub>0.5</sub>I<sub>0.5</sub>)<sub>3</sub>-MoS<sub>2</sub> phototransistors emulates optoelectronic synapse behavior using the phase segregation of halide in the perovskite films.<sup>35</sup> Separate conductance states for the application of red, green, and blue wavelengths of light was demonstrated with a hBN/Weight control layer/ WSe<sub>2</sub> optoelectronic device and the device was implemented in a spiking neural network simulation.<sup>36</sup> Although a lot of progress has been made in demonstrating optoelectronic synapse devices in ultraviolet and visible light range, the infrared regime of the broadband spectrum is still lacking adequate exploration. Two-dimensional (2D) materials are considered ideal candidates for mid infrared (MIR) optoelectronic devices because of their broadband photosensitive properties and easy integrability.<sup>37</sup> Semi-metallic graphene can absorb light from visible to terahertz wavelengths, which makes infrared photodetection possible with graphene-based devices.<sup>38</sup> But the gapless nature of graphene makes it unapplicable in emulating optoelectronic synapse characteristics. Black phosphorus (BP) has a high sensitivity to MIR due to its bandgap tunability, but its poor air stability leads to the degradation of device performance.<sup>39</sup> As a result, a metal dichalcogenide, PtTe<sub>2</sub>, is being considered as a viable 2D material for MIR optoelectronic devices due to its transition from semiconductor (monolayer) to type-II Dirac semimetal (bulk), excellent air stability, and versatile optoelectronic applications, especially in MIR sensing. 40-42 However, the dark current of a PtTe<sub>2</sub>-based photodetector is high due to its low bandgap, which reduces the

device's energy efficiency. A carefully designed heterostructure utilizing the IR sensitivity of PtTe<sub>2</sub> but maintaining a low dark current needs exploration.

In this work, we present an in-sensor artificial visual system by designing and fabricating a multiwavelength optoelectronic synapse which overcomes the shortcomings of conventional artificial visual systems by performing optical data sensing, storage, and processing in the same device. We integrate infrared sensitive PtTe<sub>2</sub>/Si as the gate electrode with UV-visible sensitive monolayer MoS<sub>2</sub> as the conduction channel in a field effect transistor (FET) configuration. Upon IR illumination, the infrared sensitive gate electrode PtTe<sub>2</sub>/Si generates electron hole pairs resulting in a photogating effect and consequently modulates the MoS<sub>2</sub> channel conductance. With UV-visible illumination, while the MoS<sub>2</sub> channel itself generates electron hole pairs and increases channel conductance, the PtTe<sub>2</sub>/Si gate electrode supplements the photocarrier generation and increases the MoS<sub>2</sub> channel conductance by the photogating effect. The emulation of all synaptic characteristics, including short term plasticity (STP), long term plasticity (LTP), stimulus intensity dependent STP to LTP transition and synaptic weight update were achieved by the device for multiple wavelengths of light from the ultraviolet (UV) to visible to near infrared (NIR) and IR light. The photo-induced conductance of the device is retained for at least 10<sup>4</sup> s by implementing hole trapping at a negative gate voltage. Distinct conductance states were obtained for four distinct wavelengths of light – 300 nm, 450 nm, 1  $\mu$ m, and 2  $\mu$ m – by modulating the number of input light pulses. Distinct photoresponsivity ranges for these four different wavelengths allowed us to obtain distinct conductance tuning curves, showing the prospect of using the same device for multicolor pattern recognition. Subsequently, we simulated a single layer artificial neural network (ANN) using the extracted weight update parameters of the optoelectronic synapse and verified the pattern recognition task for single wavelength and mixed wavelength handwritten digits. While the

network recognizes single-colored digits with high accuracy of 80%, it maintains its performance for mixed color digit recognition.

# **RESULTS AND DISCUSSION**

The schematic of the MoS<sub>2</sub> field effect transistor-based multi-wavelength optoelectronic synapse is illustrated in Figure 1a. Here, monolayer MoS<sub>2</sub> is the active channel and acts as an UVvisible sensitive material during the optical synapse operation, 10-12, 43-45 Al<sub>2</sub>O<sub>3</sub> is the back gate dielectric while p-Si/PtTe<sub>2</sub> is used as the gate electrode. The p-Si/PtTe<sub>2</sub> junction is sensitive to infrared (IR) wavelengths and is therefore chosen as the back-gate electrode to yield a multiwavelength optoelectronic synapse operation. 40-42 Both the PtTe<sub>2</sub> and MoS<sub>2</sub> films are grown by chemical vapor deposition (CVD). The details of the CVD growth and device fabrication process are provided in the experimental section. The top panel of Figure 1b shows the optical microscope image of a representative device, enlarged from the fabricated array of devices presented in the optical image at the bottom panel. The transmission electron microscope (TEM) image in Figure 1c demonstrates the continuous stacking of the gate electrode PtTe<sub>2</sub> on Si, the Al<sub>2</sub>O<sub>3</sub> gate dielectric and the monolayer MoS<sub>2</sub> channel. X-ray energy-dispersive spectra (EDS) maps in the bottom panel confirm the presence of individual elements in the stack. Figure 1d shows the Raman spectra of the whole stack with characteristic peaks for both the MoS2 and PtTe2 layers. The in plane vibrational mode  $E_g^l$  and out of plane  $A_{lg}$  modes at 110.5 cm<sup>-1</sup> and 156.9 cm<sup>-1</sup> confirm the presence of multilayer PtTe<sub>2</sub>,  $^{46}$  while  $E^{I}_{2g}$  and  $A_{Ig}$  modes of the MoS<sub>2</sub> characteristic peaks are observed at 382.4 cm<sup>-1</sup> and 400.3 cm<sup>-1</sup>, respectively. The energy difference between the two peaks is 17.9 cm<sup>-1</sup> <sup>1</sup>, corresponding to the monolayer thickness of MoS<sub>2</sub>. <sup>11, 47, 48</sup> **Figure 1e** represents the atomic force microscope (AFM) image along with the height profile across the channel, confirming the

monolayer thickness of the MoS<sub>2</sub> film. <sup>49-51</sup> The successful CVD growth of MoS<sub>2</sub> and its monolayer thickness are further confirmed by the photoluminescence spectrum in **Figure 1f** which shows a strong peak at 1.84 eV corresponding to the excitonic bandgap of the monolayer material.

To study the mechanism of light absorption of MoS<sub>2</sub> FET with PtTe<sub>2</sub>/p-Si back-gate electrode, we measured its transfer characteristics under different illumination conditions. 12, 52 Figure 2a exhibits the  $I_D$ - $V_G$  characteristics of a typical device in dark and under the light of wavelengths varying from 300 nm to 2.0 μm possessing the same intensity of 400 μW/cm<sup>2</sup>. The drain-source voltage  $(V_D)$  was kept constant at 1.0 V and the gate voltage  $(V_G)$  was swept from -5.0 V to 0 V. The threshold voltage  $(V_{Th})$  of the device shows a negative shift upon the application of different wavelengths of light, from UV (300 nm) to IR (2 µm). The maximum negative shift occurs for the wavelength of 450 nm, corresponding to the maxima of the absorption spectrum of monolayer  $MoS_2$ . 53, 54 The  $I_D$ - $V_D$  characteristics of the device, presented in **Figure S1a**, shows ohmic contact, indicating that the light induced  $V_{Th}$  shifts are not attributable to the Schottky barrier height modulation at the contacts. To understand the contribution of PtTe2 in the threshold shift characteristics, we fabricated a control device without PtTe<sub>2</sub>. Figure 2b shows the transfer characteristics of the control device with monolayer MoS<sub>2</sub> channel on p-Si back gate electrode with Al<sub>2</sub>O<sub>3</sub> gate dielectric, with no observable shift in  $V_{Th}$  for the application of infrared light (1.0  $\mu$ m, 1.5  $\mu$ m, and 2.0  $\mu$ m). <sup>43</sup> Additionally, the  $V_{Th}$  shift under the UV-visible light is lower compared to the MoS<sub>2</sub> device with PtTe<sub>2</sub>/p-Si back gate electrode. The I<sub>D</sub>-V<sub>D</sub> characteristics of the control device at different gate voltages are presented in Figure S1b. Figure 2c compares the absolute  $V_{Th}$  shifts of MoS<sub>2</sub> FETs with and without PtTe<sub>2</sub> in the gate electrode, over 5 different samples for each device type, upon illumination of the light of wavelengths 300 nm to 2 µm. The

devices with PtTe<sub>2</sub> show a significant  $V_{Th}$  shift in the infrared regime. They also show a higher  $V_{Th}$  shift in UV-visible regime compared to the control devices without PtTe<sub>2</sub>.

We measured the photo current  $(I_{Ph})$ , where  $I_{Ph} = I_{Light} - I_{Dark}$ , of the PtTe<sub>2</sub>/p-Si junction underlying the MoS<sub>2</sub> channel and Al<sub>2</sub>O<sub>3</sub> gate dielectric, with the application of 300 nm and 2.0 μm wavelengths of light of the same intensity and presented |I<sub>Ph</sub>| as a function of voltage, V in Figure 2d. As expected, the junction shows a higher photocurrent under 300 nm illumination than under illumination of 2.0 µm, since the former has higher photon energy. But surprisingly, similar results were obtained when we measured the photocurrent of the PtTe<sub>2</sub>/Si junction with the doping of the Si substrate varied from p+ condition to n+ condition, including conditions where the Si substrate is lightly doped n-type and p-type (Figure S2). This indicates that the doping of the Si substrate does not change the band alignment at the PtTe<sub>2</sub>/Si junction, confirming Fermi level pinning at the PtTe<sub>2</sub>/Si interface, possibly due to the introduction of interface traps during the direct growth of PtTe<sub>2</sub> on Si. The I-V characteristics of the PtTe<sub>2</sub>/Si junctions in Figure S2 indicate that the conduction and valence bands in Si bend upwards at the PtTe<sub>2</sub>/Si junction, as illustrated in Figure 2e-2f. At the junction, an electric field develops in the direction from p-Si to PtTe<sub>2</sub>. Figure 2e elucidates the mechanism of  $V_{Th}$  shift of the transistor when illuminated with IR light. The IR wavelengths pass through the top MoS<sub>2</sub> channel and Al<sub>2</sub>O<sub>3</sub> dielectric due to their higher bandgap and are absorbed only by the underlying semi-metallic PtTe2 layers (few layers of PtTe2 are semimetallic while monolayer PtTe<sub>2</sub> bandgap is 0.40 eV)<sup>55-57</sup>, resulting in photogenerated electron hole pairs at the PtTe<sub>2</sub>/p-Si junction. These photogenerated carriers are rapidly separated by the builtin potential of the PtTe<sub>2</sub>/p-Si junction, and holes are injected towards the PtTe<sub>2</sub>/Al<sub>2</sub>O<sub>3</sub> interface and electrons to the p-Si body. These photogenerated holes in the PtTe<sub>2</sub>/Al<sub>2</sub>O<sub>3</sub> interface create a photogating effect and shift the  $V_{Th}$  towards negative  $V_G$ . When UV-visible light is illuminated on

the device (**Figure 2f**), it is absorbed by both the top monolayer MoS<sub>2</sub> as well as the underlying PtTe<sub>2</sub>, resulting in photogenerated electron hole pairs in both layers. The photogenerated electrons in the MoS<sub>2</sub> directly contribute to the MoS<sub>2</sub> conduction channel and cause a negative  $V_{Th}$  shift. The photogenerated carriers in the underlying PtTe<sub>2</sub> are again separated by the built-in potential of PtTe<sub>2</sub>/p-Si junction, and the photogenerated holes are injected towards PtTe<sub>2</sub>/Al<sub>2</sub>O<sub>3</sub> interface recreating the aforementioned photogating effect, further enhancing the negative  $V_{Th}$  shift under UV-visible light. This clearly explains why the  $V_{Th}$  shift for UV-visible illumination is comparatively lower for the control device without PtTe<sub>2</sub> (**Figure 2c**).

To gain insight about the memory window of the transistor, we measured its transfer characteristics with varying sweep ranges of  $V_G$ . Figure 3a shows the change in device hysteresis in the transfer characteristics when the  $V_G$  sweep ranges are varied. The memory window observed for  $\pm$  1V,  $\pm$  2V,  $\pm$  3V and  $\pm$  5V sweep ranges are 0.27 V, 0.88 V, 1.68 V, and 3.92 V, respectively, *i.e.* the memory window increases with increasing  $V_G$  sweep ranges. During the forward sweep, when the gate is swept from a higher negative voltage, more holes get trapped at the MoS<sub>2</sub>/Al<sub>2</sub>O<sub>3</sub> interface shifting the  $V_{Th}$  to a more negative  $V_G$ . Subsequently, in the reverse sweep, when the gate is swept from a higher positive voltage, the trapped holes get detrapped into the MoS<sub>2</sub> channel and recombine with the channel electrons, thereby turning the device off at a higher positive  $V_G$ . These results insinuate that the device should show higher data retention at a higher negative gate voltage and the retained memory could be erased by applying a positive gate voltage. This hypothesis leads us to investigate the gate tunability of the retention of photoconductance of the device. We applied a train of 512 light pulses of wavelength 2.0  $\mu$ m, with a pulse width of 50 ms, for a constant  $V_D$  of 1.0 V and for gate voltages varying from -0.4 V to 0.1 V. The photocurrent was recorded continuously up to 600 s. The light stimulated potentiation and conductance retention of the device

at different gate voltages varying from -0.4 V to 0.1 V are shown in Figure 3b. The intensity of the 2.0 μm wavelength light used in this experiment was 866 μW/cm<sup>2</sup>. The device's conductance was normalized to the conductance at dark. We observed that the photoconductance increases for each incident light pulse, resembling the potentiation of a synapse. When the light is withdrawn, the device does not return to its initial conductance state for a long period of time. The level of conductance that the device maintains after the light pulses are withdrawn is determined by the negative gate voltage applied. The device does not maintain its conductance for long when a positive gate voltage is applied. The same experiment was then repeated for light pulses of wavelength 300 nm as shown in Figure 3c. Similar outcomes were observed since after withdrawing light, the device does not return to its initial dark current state and the level of conductance that the device maintains is determined by the negative gate voltage applied. The gate tunable potentiation and retention plots for 2.0 µm and 300 nm wavelengths of light in terms of drain-source current are presented in Figure S3a and Figure S3b respectively. The conductance retained in dark decays with time following a double exponential function  $Y = 1 + A_1 \exp(-t/\tau_1)$ +  $A_2 \exp(-t/\tau_2)$ . Here, t is the time,  $A_1$ ,  $A_2$  are initial conductance magnitudes and  $\tau_1$ ,  $\tau_2$  are the fast and slow decay time constants. The fitted plots for individual gate voltages  $V_G$  for wavelength 2.0 μm and 300 nm are presented in Figure S4 and Figure S5 respectively. We found an increase in slow decay time constant  $\tau_2$  with increasing negative  $V_G$  for both 2.0 µm and 300 nm wavelengths, which signifies higher memory retention for higher negative  $V_G$ .

STP and LTP are two cooperative functionalities essential for learning and decision making in a biological neural system.<sup>58, 59</sup> STP causes the post-synaptic conductance state to rapidly relax back to the initial conductance state when the input signal is weak, while LTP results in a long lived stable state as a result of a strong input signal. Therefore, stimulation intensity plays a vital

role in the modulation of synaptic plasticity. 60-62 Moreover, light intensity plays a huge role in the response of image sensors. Here, we report the STP to LTP transition of a single device with a change in the intensity of the optical stimulus. Figure 4a shows the intensity dependent responsivity of the device for 2.0 µm wavelength of light. The responsivity (R) is calculated according to the equation  $R = I_{Ph}/L_{inc}A$ , where  $I_{Ph}$  is the photocurrent given by  $I_{light} - I_{dark}$ ,  $L_{inc}$  is the power density of incident light and A is the channel area. With a higher light intensity, the device reaches a larger responsivity and exhibits a higher memory retention for the application of 10 light pulses of 50 ms pulse width. A clear transition from STP to LTP is observed for increasing light intensity at a constant pulse width and number of optical pulses. For a light intensity of 220 μW/cm<sup>2</sup>, the device first potentiates with applied light pulses and then decays to its initial state immediately after the light pulses are withdrawn, emulating the STP characteristics. But, with increasing light intensity, the device continues to maintain its higher conductance state after optical potentiation and exhibits LTP characteristics. Figure 4b shows similar outcomes for the application of light pulses of 300 nm wavelength. Again, the retained conductance decays with time following a double exponential function  $Y = I + B_1 \exp(-t/\tau_1) + B_2 \exp(-t/\tau_2)$ , as mentioned during the discussion of Figure 3b-c. The fitted decay plots for individual light intensities of wavelength 2.0 µm and 300 nm are presented in Figure S6a and Figure S6b respectively, showing the increase in slow decay time constant  $\tau_2$  with increasing intensity indicating the device's transition from STP to LTP.

For use of the optoelectronic synapse image sensor in neural networks, the LTP should be in the order of hundreds of seconds.  $^{63, 64}$  **Figure 5a** illustrates LTP as a function of the number of applied light pulses N, for four different wavelengths of light. During these measurements, constant  $V_D$  of 1.0 V and  $V_G$  of -0.4 V are maintained for all wavelengths. With an increasing

number of pulses from 100 to 1000, the device reaches a larger responsivity with a slower decay trend. A retention of at least 500 s is observed for 7 distinct conductance states for 4 distinct wavelengths. This result implies that the device can be used as an optoelectronic analog memory for wavelengths varying from UV (300 nm) to IR (2  $\mu$ m). The plots in terms of drain source current are included in **Figure S7**. **Figure 5b** shows an LTP of at least 10<sup>4</sup> s for 4 distinct wavelengths of light after the application of 256 light pulses. Upon fitting with the double exponential function,  $Y = I + C_1 \exp(-t/\tau_1) + C_2 \exp(-t/\tau_2)$  (**Figure S8**), we find that the slow decay time constants exceed 10<sup>4</sup> s for all four wavelengths. These results indicate the robustness of our device as a multi-wavelength optoelectronic analog memory.

The synapse's weight update characteristics are the most important requirement for the training of a neural network.<sup>63</sup> To develop a scheme for obtaining the weight update of this optoelectronic synapse, we first applied a single optical pulse of 10 s duration which potentiates the device because of the photogeneration and trapping of carriers. Then, we withdrew the light pulse and applied a single positive gate voltage pulse of 0.8 V amplitude. The positive gate voltage pulse detraps the photogenerated carriers and depresses the device to its initial state as shown in **Figure S9**. Based on this understanding, to obtain the weight update of the optoelectronic synapse, we applied a train of optical pulses to potentiate the device and positive gate voltage pulses to depress the device. The gate voltage  $V_G$  was kept constant at -0.4 V during the optical potentiation, and 256 optical pulses of 50 ms pulse width were applied. To induce depression electrically, a train of 256 voltage pulses of amplitude 0.2 V and pulse width of 30 ms was applied at the gate electrode, keeping  $V_D$  constant at 1 V throughout the experiment. The measurement was repeated for 10 cycles at four different wavelengths of 300 nm, 450 nm, 1.0  $\mu$ m and 2.0  $\mu$ m. The distinct weight update characteristics for the 4 wavelengths are shown in **Figure 6a** in terms of responsivity.

Figure S10a shows the original drain-source current for these plots. We observe 4 distinct ranges of responsivity for the 4 wavelengths, which implies that these weight update characteristics can be used to train a neural network to identify objects in UV (300 nm), visible (450 nm), near-IR (1 μm), and IR (2 μm) using the same set of synaptic devices. The cycle-to-cycle variation of the weight update plots for all four wavelengths are shown separately in Figure S10b, indicating low variability and high stability across the 10 cycles. The difference in responsivity for different wavelengths of incident light enables multi-color pattern recognition by the same optoelectronic synapse device. <sup>36, 65</sup> However, in a noisy environment where multiple wavelengths with different intensities can be incident on the device, an optical filter which makes the intensity of all wavelengths uniform will be necessary. This will allow the device to detect multi-color patterns based on the distinct responsivities for 300 nm, 450 nm, 1 µm and 2 µm wavelengths. A high dynamic range, given by the ratio of the maximum to minimum responsivity for a particular weight update ensures high accuracy in pattern recognition with a neural network. Figure 6b shows the dynamic range for all 4 wavelengths across the 10 cycles, varying from ~10 for IR light to ~250 for visible light. The nonlinearity factor (NLF) is also critical in determining the accuracy of learning. The NLF for the potentiation  $(\alpha_p)$  and depression  $(\alpha_d)$  regimes was calculated using the equation  $\alpha_{p,d} = 1.726 / (A_{p,d} + 0.162)$  where  $A_{p,d}$  is the parameter that controls the nonlinear behavior of the weight update, deduced from the non-linear curve fitting of potentiation and depression. 66-68 The extracted NLF for both potentiation and depression are plotted in Figure 6c.

Following the weight update measurements, we developed a single layer NN using the extracted device parameters for single wavelength and mixed-wavelength pattern recognition tasks. We utilize the device parameters like dynamic range, NLF and conductances for the 4 different wavelengths to simulate the NN. This NN has the ability to identify the target number

from the mixed wavelength pattern. Here, the target number is buried in the mixed pattern and is known as the inside digit. Further, the NN also has the ability to recognize the remaining part of the mixed pattern which is called the complement digit. We test the NN for 3 mixed patterns viz., 3 in 8, 1 in 7, and 1 in 4 where the task of the NN is to recognize pattern '3' in '8', '1' in '7' and '1'in '4'. The MNIST dataset was used for training and testing the NN. However, a simple modification is executed to create a dataset where the original size of the image (28 × 28) is preserved, and wavelength dependent color is appended to the image. Therefore, while testing the NN, the network is able to recognize the inside and complement digits of corresponding wavelengths. The schematic of the NN is shown in Figure 6d. The input pixel arrays of the same image for variable wavelengths are stacked as shown in the figure. The weight matrix comprises the wavelength dependent conductance values which is then utilized to implement vector-matrix multiplication. The output layer consists of 8 sigmoid-activated neurons. The training dataset consists of 120,000 (30000 ×4) single wavelength images. For 3 in 8 recognition tasks, the training dataset consists of both '3' and '8' single patterns in 4 different wavelengths. We prepared test datasets which contains 800 test images with single and mixed patterns. The network was trained for 1000 epochs. At the end of each epoch, the cost is calculated and plotted as a function of epoch number as shown in Figure 6e. After the cost function estimation, the weight update is executed accordingly to reduce the cost function for subsequent training epochs.<sup>36</sup> Additionally, we estimate the recognition after each training epoch and the recognition accuracy is plotted as the function of epoch number as shown in Figure 6f. We observe recognition accuracy of '3' in '8' patterns to be ~80 %. The recognition accuracies of '1' in '7' and '1' in '4' patterns are shown in Figure S11. The activation values of each neuron in cases of single patterns is presented in Figure 6g, where we observe high activation values for both '3' and '8' neurons corresponding to single wavelength,

indicating the presence of pattern '3' in the number '8'. The inset of the figure shows the test image. Likewise, we plot activation functions of various mixed wavelength patterns as shown in **Figure 6h** with the test images (Inset: corresponding mixed-color pattern). For the test images where the inside digit is '3' in 2 µm wavelength and the complement is '8' in 300 nm wavelength, we observe high activation values for 3 different neurons. Here, both '3' and '8' neurons of 2 µm wavelength show high values because the inside digit is '3' can either be a stand-alone '3' pattern or a part of '8'. The complement specifically belongs to pattern '8' which induces high activation value in the 300 nm '8' neuron. To attest to the multi-wavelength functionality of our synapses we have presented activation values of test images of all possible combinations of wavelengths as shown in the inset of the figure. In addition to this, we perform the testing phase on other mixed color patterns ('1' in '4' and, '1' in '7') and the corresponding activation values are shown in **Figure S11**.

#### **CONCLUSION**

An intelligent artificial visual system is developed with a multi-wavelength optoelectronic synapse and ANN for real time pattern recognition. In typical artificial visual systems, the sensing unit is physically separated from the processing unit while our reported in-sensor computing system can process the visual information by the sensory terminal to avoid redundant raw data. Additionally, the device is tested for single colored and multi-colored pattern recognition with UV, visible, NIR, and IR wavelengths of light, simultaneously. The reported artificial visual system can advance machine vision technology by increasing the processing efficiency and the accuracy of subsequent image recognition.

# **METHODS**

Materials and Device fabrication. 6.0 nm of Pt was deposited by e-beam evaporation on a Si substrate. The Pt-deposited substrate was placed at the center zone of the quartz tube inside a thermal furnace (Blue M Mini-Mite, Lindberg), and the tellurium (Te) powder (CAS No. 13494-80-9, 200 mesh, 99.8%, Sigma-Aldrich. Inc.) in an alumina boat was placed at the upstream side of the furnace. The quartz tube containing the Pt deposited substrate and the Te powder in an alumina boat was evacuated to a basal pressure of under 15 mTorr and purged with argon (Ar) gas to remove oxygen and organic residuals. Then, the furnace was heated up to the growth temperature of 400 °C in 50 min, and the temperature was maintained for an additional 50 min before its natural cool-down to ambient temperature. During the PtTe<sub>2</sub> growth reaction, the flow rate of Ar gas was maintained to be ~ 200 standard cubic centimeters per minute (SCCM) at a pressure of ~ 80 mTorr. 250 nm of Au was deposited by e-beam evaporation as a contact for PtTe<sub>2</sub> followed by 200 nm of SiO<sub>2</sub> deposition underneath. 20 nm of Al<sub>2</sub>O<sub>3</sub> was deposited by atomic layer deposition (ALD) as a gate dielectric. The source/drain contacts were patterned and deposited on the by e-beam evaporation of Ni/Au (60 nm/40 nm). High quality and a large area of monolayer  $MoS_2$  was grown on a separate  $2.0 \times 2.0$  cm<sup>2</sup> Si/SiO<sub>2</sub> substrate by chemical vapor deposition (CVD) in an MTI furnace using MoS<sub>2</sub> powder as a precursor. MoS<sub>2</sub> powder precursor of molecular weight 160.07 was purchased from Sigma Aldrich. 500 mg of MoS<sub>2</sub> powder was loaded into a quartz boat and placed upstream at the center of the heating zone. In the downstream, Si/SiO<sub>2</sub> substrate was placed at a distance of 7.0 cm away from the precursor. The system was pumped down to 15 mT pressure and then 1553 sccm flow of carrier gas Ar was supplied to bring the pressure at a stable 2.0 Torr. For 30 mins of growth time at 950 °C temperature, the Si/SiO<sub>2</sub> substrate was completely covered with a monolayer film of MoS<sub>2</sub>. The MoS<sub>2</sub> film was then spin coated with a thin layer of poly (methyl methacrylate) (PMMA) and kept at room temperature

overnight. Using a razor blade, the edges of the PMMA coated sample was scratched and floated on buffer oxide etchant (BOE, 40% NH<sub>4</sub>F/49% HF, 6:1 v/v in water) for 6 h. The etchant seeped through the SiO<sub>2</sub> underneath and the MoS<sub>2</sub> film was released from the substrate along with the PMMA supporting layer. The floating MoS<sub>2</sub> film with PMMA was then transferred to a deionized water bath and kept for 20 mins. This water rinsing process was repeated three times to remove the acid remnant. The MoS<sub>2</sub> film with PMMA was then transferred on the target p-Si/PtTe<sub>2</sub>/Al<sub>2</sub>O<sub>3</sub> substrate and dried for 15 min. The sample was heated on a hot plate at 220 °C for 5 min and the PMMA layer was removed by immersing the sample in acetone for 3 h. The MoS<sub>2</sub> film was patterned by photolithography and etched in O<sub>2</sub> plasma.

Device Characterization The cross-sectional structural analysis of the device was performed using JEOL ARM 200F Cs-corrected TEM (operation voltage: 200 kV). The samples for the cross-sectional STEM were prepared by focused ion beam (FIB; Quanta 2D FEG, FEI)-based milling and lift-out techniques using gallium (Ga) ion beam (30 keV) and a micro-manipulator (Omniprobe). Raman and photoluminescence spectroscopy was performed on Horiba LabRAM HR Evolution Nano Spectrometer with excitation of 532 nm. Electrical characterizations were performed on a Micromanipulator probe station (room temperature, in the air) using a Keysight B1500A Semiconductor Device Analyzer. Newport Quartz Tungsten Halogen lamp was used as the light source with Newport CS130B-3-MC monochromator to split the light into specific wavelengths. Light intensity was measured by THORLABS S401C thermal power sensor. Newport 75150 Apex Optical Chopper System was used to obtain the desired frequency of light pulses.

## **ACKNOWLEDGEMENTS**

T. Roy conceived the project and directed it. M. M. Islam performed the MoS<sub>2</sub> synthesis and S. Han did the PtTe<sub>2</sub> synthesis. Device fabrication was performed by M. M. Islam and D. Dev and M. M. Islam performed the device characterization. T. Bae and H. Chung performed the TEM of the fabricated device. M. M. Islam and D. Dev performed the AFM of CVD grown monolayer MoS<sub>2</sub>. A. Krishnaprasad and B. Wu performed the object identification with neural network simulation under the guidance of J. Touma. M. M. Islam, A. Krishnaprasad and T. Roy wrote the manuscript with inputs from all authors. This work is supported by NSF-ECCS-1845331 (CAREER) and AFOSR through award number FA8651-20-1-0008.

## **Conflicts of Interest**

The authors declare no conflicts of interest.

#### ASSOCIATED CONTENT

**Supporting Information**  $I_D$ - $V_D$  characteristics of p-Si/PtTe<sub>2</sub>/Al<sub>2</sub>O<sub>3</sub>/MoS<sub>2</sub> device and p-Si/Al<sub>2</sub>O<sub>3</sub>/MoS<sub>2</sub> control device in dark, I-V characteristics in dark and under 300 nm and 2.0 μm wavelengths of light of different doped PtTe<sub>2</sub>/Si junction. gate dependence in terms of current with 2.0 μm and 300 nm light, double exponential curve fitting of gate-dependence with 2.0 μm and 300 nm, double exponential curve fitting of transition of the device from short term potentiation to long term potentiation at different light intensities, long term potentiation (LTP) with 2.0 μm,  $1.0 \mu m$ , 300 nm and 450 nm light, double exponential curve fitting of long term retention in terms of current for  $10^4$  s, carrier trapping with single light pulse and de trapping with sin single positive gate voltage pulse, weight update measurement in terms of current, cycle to cycle variation of the weight update measurement in terms of current, single wavelength and mixed-wavelength pattern recognition.

#### REFERENCES

- 1. Zhou, F.; Zhou, Z.; Chen, J.; Choy, T. H.; Wang, J.; Zhang, N.; Lin, Z.; Yu, S.; Kang, J.; Wong, H.-S. P., Optoelectronic resistive random access memory for neuromorphic vision sensors. *Nature nanotechnology* **2019**, *14* (8), 776-782.
- 2. Mennel, L.; Symonowicz, J.; Wachter, S.; Polyushkin, D. K.; Molina-Mendoza, A. J.; Mueller, T., Ultrafast machine vision with 2D material neural network image sensors. *Nature* **2020**, *579* (7797), 62-66.
- 3. Radovic, A.; Williams, M.; Rousseau, D.; Kagan, M.; Bonacorsi, D.; Himmel, A.; Aurisano, A.; Terao, K.; Wongjirad, T., Machine learning at the energy and intensity frontiers of particle physics. *Nature* **2018**, *560* (7716), 41-48.
- 4. LeCun, Y.; Bengio, Y.; Hinton, G., Deep learning. *nature* **2015**, *521* (7553), 436-444.
- 5. Zhang, M.; Fan, Z.; Jiang, X.; Zhu, H.; Chen, L.; Xia, Y.; Yin, J.; Liu, X.; Sun, Q.; Zhang, D. W., MoS2-based charge-trapping synaptic device with electrical and optical modulated conductance. *Nanophotonics* **2020**, *9* (8), 2475-2486.
- 6. Zhou, F.; Chai, Y., Near-sensor and in-sensor computing. *Nature Electronics* **2020**, *3* (11), 664-671.
- 7. Luo, Z.-D.; Xia, X.; Yang, M.-M.; Wilson, N. R.; Gruverman, A.; Alexe, M., Artificial optoelectronic synapses based on ferroelectric field-effect enabled 2D transition metal dichalcogenide memristive transistors. *ACS nano* **2019**, *14* (1), 746-754.
- 8. Agnus, G.; Zhao, W.; Derycke, V.; Filoramo, A.; Lhuillier, Y.; Lenfant, S.; Vuillaume, D.; Gamrat, C.; Bourgoin, J. P., Two-terminal carbon nanotube programmable devices for adaptive architectures. *Advanced Materials* **2010**, *22* (6), 702-706.
- 9. Shao, L.; Wang, H.; Yang, Y.; He, Y.; Tang, Y.; Fang, H.; Zhao, J.; Xiao, H.; Liang, K.; Wei, M., Optoelectronic properties of printed photogating carbon nanotube thin film transistors and their application for light-stimulated neuromorphic devices. *ACS applied materials & interfaces* **2019**, *11* (12), 12161-12169.
- 10. Wang, S.; Hou, X.; Liu, L.; Li, J.; Shan, Y.; Wu, S.; Zhang, D. W.; Zhou, P., A photoelectric-stimulated MoS2 transistor for neuromorphic engineering. *Research* **2019**, *2019*.
- 11. He, H. K.; Yang, R.; Zhou, W.; Huang, H. M.; Xiong, J.; Gan, L.; Zhai, T. Y.; Guo, X., Photonic potentiation and electric habituation in ultrathin memristive synapses based on monolayer MoS2. *Small* **2018**, *14* (15), 1800079.
- 12. Islam, M. M.; Dev, D.; Krishnaprasad, A.; Tetard, L.; Roy, T., Optoelectronic synapse using monolayer MoS 2 field effect transistors. *Scientific reports* **2020**, *10* (1), 1-9.
- 13. Wang, S.; Chen, C.; Yu, Z.; He, Y.; Chen, X.; Wan, Q.; Shi, Y.; Zhang, D. W.; Zhou, H.; Wang, X., A MoS2/PTCDA hybrid heterojunction synapse with efficient photoelectric dual modulation and versatility. *Advanced Materials* **2019**, *31* (3), 1806227.
- 14. John, R. A.; Liu, F.; Chien, N. A.; Kulkarni, M. R.; Zhu, C.; Fu, Q.; Basu, A.; Liu, Z.; Mathews, N., Synergistic gating of electro-iono-photoactive 2D chalcogenide neuristors: coexistence of hebbian and homeostatic synaptic metaplasticity. *Advanced Materials* **2018**, *30* (25), 1800220.
- 15. Tran, M. D.; Kim, H.; Kim, J. S.; Doan, M. H.; Chau, T. K.; Vu, Q. A.; Kim, J. H.; Lee, Y. H., Two-terminal multibit optical memory via van der Waals heterostructure. *Advanced Materials* **2019**, *31* (7), 1807075.

- 16. Jiang, J.; Hu, W.; Xie, D.; Yang, J.; He, J.; Gao, Y.; Wan, Q., 2D electric-double-layer phototransistor for photoelectronic and spatiotemporal hybrid neuromorphic integration. *Nanoscale* **2019**, *11* (3), 1360-1369.
- 17. Yin, S.; Song, C.; Sun, Y.; Qiao, L.; Wang, B.; Sun, Y.; Liu, K.; Pan, F.; Zhang, X., Electric and light dual-gate tunable MoS2 memtransistor. *ACS applied materials & interfaces* **2019**, *11* (46), 43344-43350.
- 18. Sun, Y.; Ding, Y.; Xie, D.; Xu, J.; Sun, M.; Yang, P.; Zhang, Y., Optically stimulated synaptic transistor based on MoS 2/quantum dots mixed-dimensional heterostructure with gate-tunable plasticity. *Optics Letters* **2021**, *46* (7), 1748-1751.
- 19. Xu, M.; Xu, T.; Yu, A.; Wang, H.; Wang, H.; Zubair, M.; Luo, M.; Shan, C.; Guo, X.; Wang, F., Optoelectronic Synapses Based on Photo-Induced Doping in MoS2/h-BN Field-Effect Transistors. *Advanced Optical Materials* **2021**, *9* (20), 2100937.
- 20. Abnavi, A.; Ahmadi, R.; Hasani, A.; Fawzy, M.; Mohammadzadeh, M. R.; De Silva, T.; Yu, N.; Adachi, M. M., Free-Standing Multilayer Molybdenum Disulfide Memristor for Brain-Inspired Neuromorphic Applications. *ACS Applied Materials & Interfaces* **2021**, *13* (38), 45843-45853.
- 21. Ahmed, T.; Kuriakose, S.; Mayes, E. L.; Ramanathan, R.; Bansal, V.; Bhaskaran, M.; Sriram, S.; Walia, S., Optically stimulated artificial synapse based on layered black phosphorus. *Small* **2019**, *15* (22), 1900966.
- 22. Qin, S.; Wang, F.; Liu, Y.; Wan, Q.; Wang, X.; Xu, Y.; Shi, Y.; Wang, X.; Zhang, R., A light-stimulated synaptic device based on graphene hybrid phototransistor. *2D Materials* **2017**, *4* (3), 035022.
- 23. Sun, J.; Oh, S.; Choi, Y.; Seo, S.; Oh, M. J.; Lee, M.; Lee, W. B.; Yoo, P. J.; Cho, J. H.; Park, J. H., Optoelectronic synapse based on igzo-alkylated graphene oxide hybrid structure. *Advanced Functional Materials* **2018**, *28* (47), 1804397.
- 24. Lee, M.; Lee, W.; Choi, S.; Jo, J. W.; Kim, J.; Park, S. K.; Kim, Y. H., Brain-inspired photonic neuromorphic devices using photodynamic amorphous oxide semiconductors and their persistent photoconductivity. *Advanced Materials* **2017**, *29* (28), 1700951.
- 25. Yu, J.; Liang, L.; Hu, L.; Duan, H.; Wu, W.; Zhang, H.; Gao, J.; Zhuge, F.; Chang, T.; Cao, H., Optoelectronic neuromorphic thin-film transistors capable of selective attention and with ultra-low power dissipation. *Nano Energy* **2019**, *62*, 772-780.
- 26. Zhao, L.; Fan, Z.; Cheng, S.; Hong, L.; Li, Y.; Tian, G.; Chen, D.; Hou, Z.; Qin, M.; Zeng, M., An artificial optoelectronic synapse based on a photoelectric memcapacitor. *Advanced Electronic Materials* **2020**, *6* (2), 1900858.
- 27. Kim, M. K.; Lee, J. S., Synergistic Improvement of Long-Term Plasticity in Photonic Synapses Using Ferroelectric Polarization in Hafnia-Based Oxide-Semiconductor Transistors. *Advanced Materials* **2020**, *32* (12), 1907826.
- 28. Tan, H.; Liu, G.; Yang, H.; Yi, X.; Pan, L.; Shang, J.; Long, S.; Liu, M.; Wu, Y.; Li, R., Light-gated memristor with integrated logic and memory functions. ACS Nano 11, 11298 (2017).
- 29. Tan, H.; Liu, G.; Zhu, X.; Yang, H.; Chen, B.; Chen, X.; Shang, J.; Lu, W. D.; Wu, Y.; Li, R. W., An optoelectronic resistive switching memory with integrated demodulating and arithmetic functions. *Advanced Materials* **2015**, *27* (17), 2797-2803.
- 30. Qian, C.; Oh, S.; Choi, Y.; Kim, J.-H.; Sun, J.; Huang, H.; Yang, J.; Gao, Y.; Park, J.-H.; Cho, J. H., Solar-stimulated optoelectronic synapse based on organic heterojunction with

- linearly potentiated synaptic weight for neuromorphic computing. *Nano Energy* **2019**, *66*, 104095.
- 31. Ham, S.; Choi, S.; Cho, H.; Na, S. I.; Wang, G., Photonic Organolead Halide Perovskite Artificial Synapse Capable of Accelerated Learning at Low Power Inspired by Dopamine-Facilitated Synaptic Activity. *Advanced Functional Materials* **2019**, *29* (5), 1806646.
- 32. Tian, H.; Wang, X.; Wu, F.; Yang, Y.; Ren, T.-L. High Performance 2D Perovskite/Graphene Optical Synapses as Artificial Eyes. Proceedings from the International Electron Devices Meeting, IEDM, San Francisco, CA, December 1–5, 2018; IEEE: San Francisco, CA, USA, 2018 of Conference; pp 38.6.1–38.6.4.
- 33. Pradhan, B.; Das, S.; Li, J.; Chowdhury, F.; Cherusseri, J.; Pandey, D.; Dev, D.; Krishnaprasad, A.; Barrios, E.; Towers, A., Ultrasensitive and ultrathin phototransistors and photonic synapses using perovskite quantum dots grown from graphene lattice. *Science advances* **2020**, *6* (7), eaay5225.
- 34. Hong, S.; Cho, H.; Kang, B. H.; Park, K.; Akinwande, D.; Kim, H. J.; Kim, S., Neuromorphic Active Pixel Image Sensor Array for Visual Memory. *ACS nano* **2021**, *15* (9), 15362-15370.
- 35. Hong, S.; Choi, S. H.; Park, J.; Yoo, H.; Oh, J. Y.; Hwang, E.; Yoon, D. H.; Kim, S., Sensory Adaptation and Neuromorphic Phototransistors Based on CsPb (Br1–x I x) 3 Perovskite and MoS2 Hybrid Structure. *ACS nano* **2020**, *14* (8), 9796-9806.
- 36. Seo, S.; Jo, S.-H.; Kim, S.; Shim, J.; Oh, S.; Kim, J.-H.; Heo, K.; Choi, J.-W.; Choi, C.; Oh, S., Artificial optic-neural synapse for colored and color-mixed pattern recognition. *Nature Communications* **2018**, *9* (1), 1-8.
- 37. Long, M.; Gao, A.; Wang, P.; Xia, H.; Ott, C.; Pan, C.; Fu, Y.; Liu, E.; Chen, X.; Lu, W., Room temperature high-detectivity mid-infrared photodetectors based on black arsenic phosphorus. *Science advances* **2017**, *3* (6), e1700589.
- 38. Wang, X.; Cheng, Z.; Xu, K.; Tsang, H. K.; Xu, J.-B., High-responsivity graphene/silicon-heterostructure waveguide photodetectors. *Nature Photonics* **2013**, *7* (11), 888-891.
- 39. Chen, X.; Lu, X.; Deng, B.; Sinai, O.; Shao, Y.; Li, C.; Yuan, S.; Tran, V.; Watanabe, K.; Taniguchi, T., Widely tunable black phosphorus mid-infrared photodetector. *Nature communications* **2017**, *8* (1), 1-7.
- 40. Lai, J.; Ma, J.; Liu, Y.; Zhang, K.; Zhuo, X.; Chen, J.; Zhou, S.; Sun, D., Photocurrent response of type-II Dirac semimetal PtTe2. 2D Materials **2020**, 7 (3), 034003.
- 41. Zeng, L.; Wu, D.; Jie, J.; Ren, X.; Hu, X.; Lau, S. P.; Chai, Y.; Tsang, Y. H., Van der Waals epitaxial growth of mosaic-like 2D platinum ditelluride layers for room-temperature midinfrared photodetection up to 10.6 μm. *Advanced Materials* **2020**, *32* (52), 2004412.
- 42. Shawkat, M. S.; Hafiz, S. B.; Islam, M. M.; Mofid, S. A.; Al Mahfuz, M. M.; Biswas, A.; Chung, H.-S.; Okogbue, E.; Ko, T.-J.; Chanda, D., Scalable Van der Waals Two-Dimensional PtTe2 Layers Integrated onto Silicon for Efficient Near-to-Mid Infrared Photodetection. *ACS applied materials & interfaces* **2021**, *13* (13), 15542-15550.
- 43. Han, P.; Adler, E. R.; Liu, Y.; St Marie, L.; El Fatimy, A.; Melis, S.; Van Keuren, E.; Barbara, P., Ambient effects on photogating in MoS2 photodetectors. *Nanotechnology* **2019**, *30* (28), 284004.
- 44. Kim, S.-G.; Kim, S.-H.; Park, J.; Kim, G.-S.; Park, J.-H.; Saraswat, K. C.; Kim, J.; Yu, H.-Y., Infrared detectable MoS2 phototransistor and its application to artificial multilevel optic-neural synapse. *ACS nano* **2019**, *13* (9), 10294-10300.

- 45. Dodda, A.; Jayachandran, D.; Radhakrishnan, S. S.; Das, S., A Bio-inspired and Low-power 2D Machine Vision with Adaptive Machine Learning and Forgetting, **2021**, rs-258246, Research Square, https://doi.org/10.21203/rs.3.rs-258246/v1 (Feb 24<sup>th</sup>, 2021).
- 46. Ma, H.; Chen, P.; Li, B.; Li, J.; Ai, R.; Zhang, Z.; Sun, G.; Yao, K.; Lin, Z.; Zhao, B., Thickness-tunable synthesis of ultrathin type-II Dirac semimetal PtTe2 single crystals and their thickness-dependent electronic properties. *Nano letters* **2018**, *18* (6), 3523-3529.
- 47. Lee, C.; Yan, H.; Brus, L. E.; Heinz, T. F.; Hone, J.; Ryu, S., Anomalous lattice vibrations of single-and few-layer MoS2. *ACS nano* **2010**, *4* (5), 2695-2700.
- 48. Singh, A. K.; Andleeb, S.; Singh, J.; Dung, H. T.; Seo, Y.; Eom, J., Ultraviolet-Light-Induced Reversible and Stable Carrier Modulation in MoS2 Field-Effect Transistors. *Advanced Functional Materials* **2014**, *24* (45), 7125-7132.
- 49. Giannazzo, F.; Bosi, M.; Fabbri, F.; Schilirò, E.; Greco, G.; Roccaforte, F., Direct Probing of Grain Boundary Resistance in Chemical Vapor Deposition-Grown Monolayer MoS2 by Conductive Atomic Force Microscopy. *physica status solidi (RRL)–Rapid Research Letters* **2020**, *14* (2), 1900393.
- 50. Yakubovsky, D. I.; Stebunov, Y. V.; Kirtaev, R. V.; Ermolaev, G. A.; Mironov, M. S.; Novikov, S. M.; Arsenin, A. V.; Volkov, V. S., Ultrathin and ultrasmooth gold films on monolayer MoS2. *Advanced Materials Interfaces* **2019**, *6* (13), 1900196.
- 51. Wang, Y.; Zhang, L.; Su, C.; Xiao, H.; Lv, S.; Zhang, F.; Sui, Q.; Jia, L.; Jiang, M., Direct Observation of Monolayer MoS2 Prepared by CVD Using In-Situ Differential Reflectance Spectroscopy. *Nanomaterials* **2019**, *9* (11), 1640.
- 52. Wu, J. Y.; Chun, Y. T.; Li, S.; Zhang, T.; Wang, J.; Shrestha, P. K.; Chu, D., Broadband MoS2 Field-Effect Phototransistors: Ultrasensitive Visible-Light Photoresponse and Negative Infrared Photoresponse. *Advanced Materials* **2018**, *30* (7), 1705880.
- 53. Castellanos-Gomez, A.; Quereda, J.; van der Meulen, H. P.; Agraït, N.; Rubio-Bollinger, G., Spatially resolved optical absorption spectroscopy of single-and few-layer MoS2 by hyperspectral imaging. *Nanotechnology* **2016**, *27* (11), 115705.
- 54. Yalon, E.; Aslan, O. B.; Smithe, K. K.; McClellan, C. J.; Suryavanshi, S. V.; Xiong, F.; Sood, A.; Neumann, C. M.; Xu, X.; Goodson, K. E., Temperature-dependent thermal boundary conductance of monolayer MoS2 by Raman thermometry. *ACS applied materials & interfaces* **2017**, *9* (49), 43013-43020.
- 55. Cheng, P. K.; Tang, C. Y.; Wang, X. Y.; Ma, S.; Long, H.; Tsang, Y. H., Passively Q-switched Ytterbium-doped fiber laser based on broadband multilayer Platinum Ditelluride (PtTe 2) saturable absorber. *Scientific reports* **2019**, *9* (1), 1-7.
- 56. Villaos, R. A. B.; Crisostomo, C. P.; Huang, Z.-Q.; Huang, S.-M.; Padama, A. A. B.; Albao, M. A.; Lin, H.; Chuang, F.-C., Thickness dependent electronic properties of Pt dichalcogenides. *npj 2D Materials and Applications* **2019**, *3* (1), 1-8.
- 57. Li, J.; Kolekar, S.; Ghorbani-Asl, M.; Lehnert, T.; Biskupek, J.; Kaiser, U.; Krasheninnikov, A. V.; Batzill, M., Layer-Dependent Band Gaps of Platinum Dichalcogenides. *ACS Nano* **2021**, *15* (8), 13249-13259.
- 58. Ohno, T.; Hasegawa, T.; Tsuruoka, T.; Terabe, K.; Gimzewski, J. K.; Aono, M., Shortterm plasticity and long-term potentiation mimicked in single inorganic synapses. *Nature materials* **2011**, *10* (8), 591-595.
- 59. Duan, H.; Javaid, K.; Liang, L.; Huang, L.; Yu, J.; Zhang, H.; Gao, J.; Zhuge, F.; Chang, T.-C.; Cao, H., Broadband Optoelectronic Synaptic Thin-Film Transistors Based on

- Oxide Semiconductors. *physica status solidi (RRL)–Rapid Research Letters* **2020**, *14* (4), 1900630.
- 60. Zhang, J.; Sun, H.; Li, Y.; Wang, Q.; Xu, X.; Miao, X., AgInSbTe memristor with gradual resistance tuning. *Applied Physics Letters* **2013**, *102* (18), 183513.
- 61. Feng, P.; Xu, W.; Yang, Y.; Wan, X.; Shi, Y.; Wan, Q.; Zhao, J.; Cui, Z., Printed Neuromorphic Devices Based on Printed Carbon Nanotube Thin-Film Transistors. *Advanced Functional Materials* **2017**, *27* (5), 1604447.
- 62. Du, C.; Ma, W.; Chang, T.; Sheridan, P.; Lu, W. D., Biorealistic implementation of synaptic functions with oxide memristors through internal ionic dynamics. *Advanced Functional Materials* **2015**, *25* (27), 4290-4299.
- 63. Yu, S., Neuro-inspired computing with emerging nonvolatile memorys. *Proceedings of the IEEE* **2018**, *106* (2), 260-285.
- 64. Zhou, F.; Zhou, Z.; Chen, J.; Choy, T. H.; Wang, J.; Zhang, N.; Lin, Z.; Yu, S.; Kang, J.; Wong, H. S. P.; Chai, Y., Optoelectronic resistive random access memory for neuromorphic vision sensors. *Nature Nanotechnology* **2019**, *14* (8), 776-782.
- 65. Zhang, J.; Lu, Y.; Dai, S.; Wang, R.; Hao, D.; Zhang, S.; Xiong, L.; Huang, J., Retina-inspired organic heterojunction-based optoelectronic synapses for artificial visual systems. *Research* **2021**, *2021*.
- 66. Jerry, M.; Chen, P. Y.; Zhang, J. C.; Sharma, P.; Ni, K.; Yu, S. M.; Datta, S. Ferroelectric FET Analog Synapse for Acceleration of Deep Neural Network Training. Proceedings from the International Electron Devices Meeting, IEDM, San Francisco, CA, December 2–6, 2017; IEEE: San Francisco, CA, USA, 2017 of Conference; pp 6.2.1–6.2.4.
- 67. Chen, P. Y.; Lin, B.; Wang, I. T.; Hou, T. H.; Ye, J.; Vrudhula, S.; Seo, J. S.; Cao, Y.; Yu, S. Mitigating Effects of Non-Ideal Synaptic Device Characteristics for on-Chip Learning. Proceedings from the 2015 IEEE/ACM International Conference on Computer-Aided Design, ICCAD 2015, Austin, TX, November 2–6, 2015; IEEE: New York, 2015; pp 194–199.
- 68. Yu, S.; Chen, P. Y.; Cao, Y.; Xia, L.; Wang, Y.; Wu, H. Scaling up Resistive Synaptic Arrays for Neuro-Inspired Architecture: Challenges and Prospect. Proceedings from the International Electron Devices Meeting, IEDM, San Francisco, CA, December 3–7, 2016; IEEE: New York, 2016; pp 17.3.1–17.3.4.

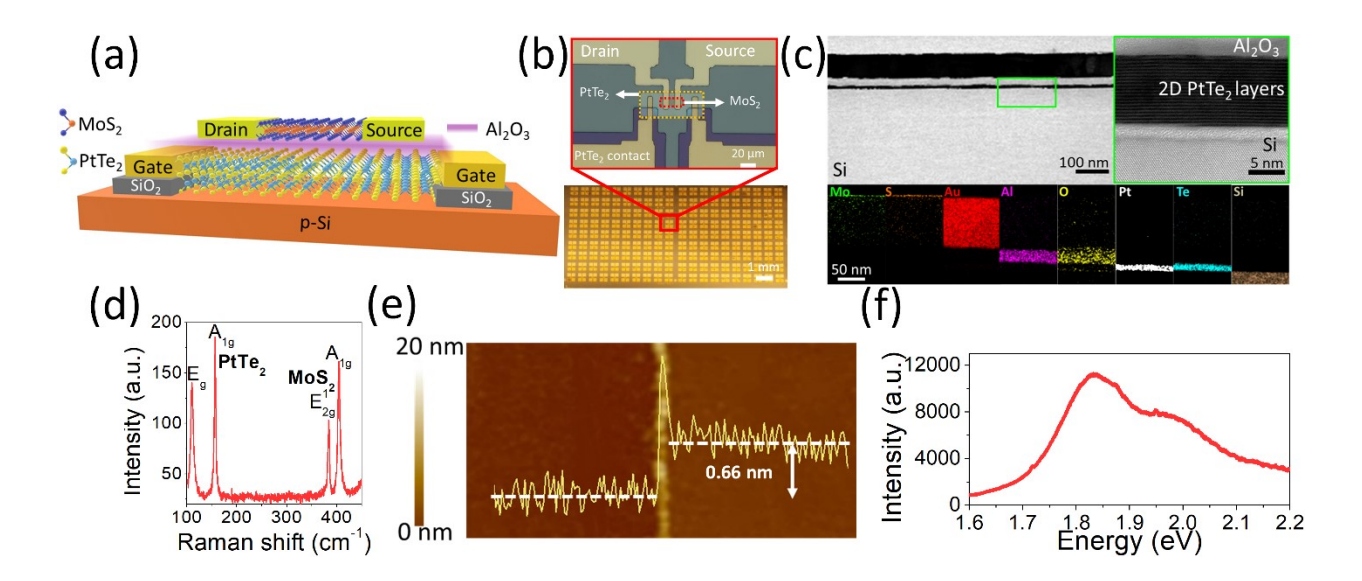
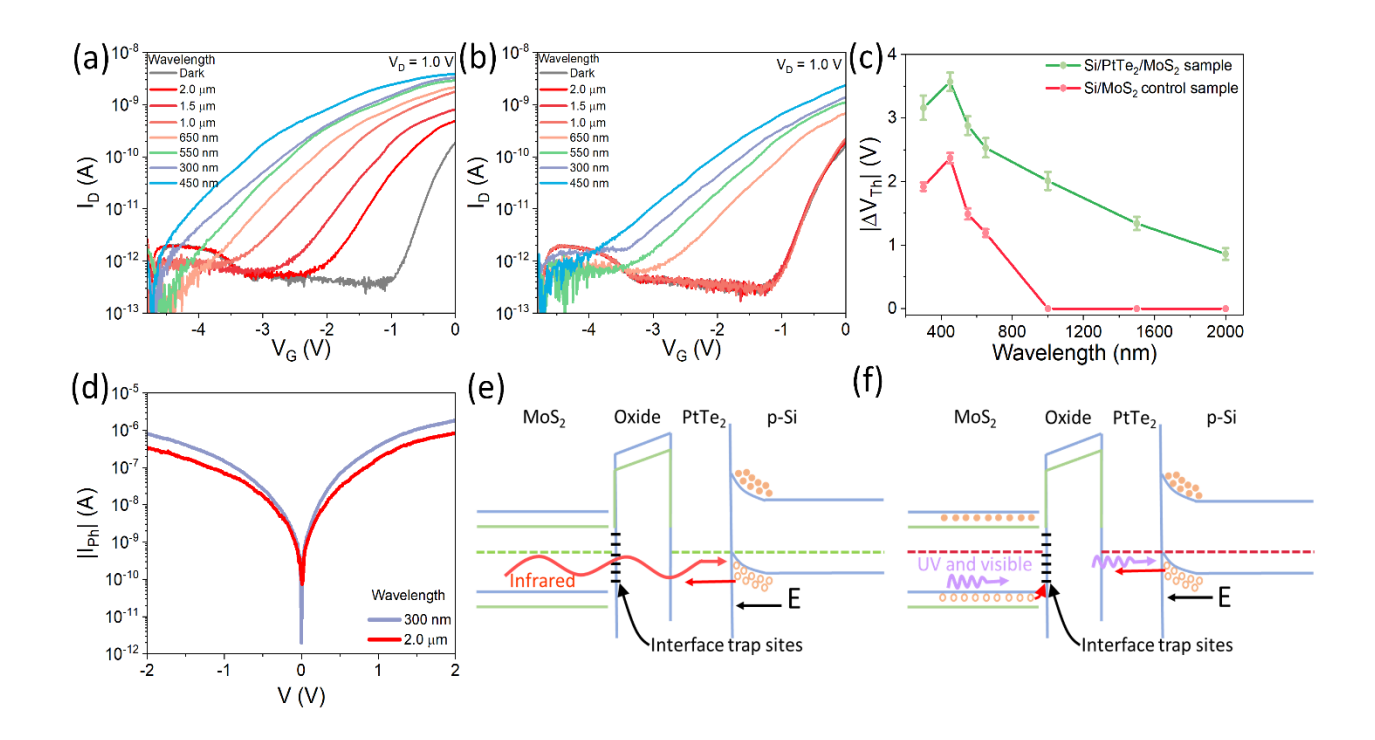
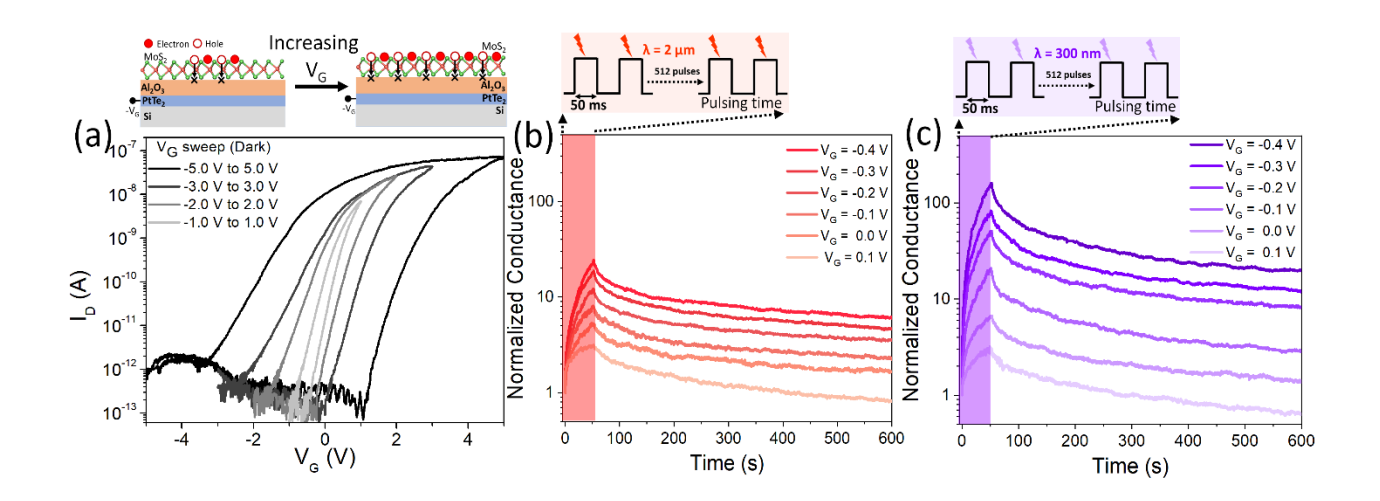


Figure 1. (a) Schematic diagram (not to scale) of multi-wavelength optoelectronic synapse. (b) Optical image of the chip (bottom panel) and optical microscope image (top panel) of single optoelectronic synapse device (c) TEM image and EDS map (bottom panel) of multi-wavelength optoelectronic synapse. (d) Raman spectrum of the whole stack shows corresponding PtTe<sub>2</sub> and MoS<sub>2</sub> peaks. (e) AFM image (f) Photoluminescence spectrum of monolayer MoS<sub>2</sub> channel.



**Figure 2.**  $I_D$ - $V_G$  characteristics showing the shift in threshold voltage with the application of light of wavelengths from 300 nm to 2 μm of (a) Si/PtTe<sub>2</sub>/Al<sub>2</sub>O<sub>3</sub>/MoS<sub>2</sub> device and (b) Si/Al<sub>2</sub>O<sub>3</sub>/MoS<sub>2</sub> device at a constant V<sub>D</sub> of 1.0 V. (c) Comparison of  $|\Delta V_{Th}|$  as a function of light wavelength for Si/PtTe<sub>2</sub>/Al<sub>2</sub>O<sub>3</sub>/MoS<sub>2</sub> device and Si/Al<sub>2</sub>O<sub>3</sub>/MoS<sub>2</sub> device. (d) Absolute photocurrent of PtTe<sub>2</sub>/Si junction under illumination of UV (300 nm) and IR (2.0 μm) light. Energy band diagram of the p-Si/PtTe<sub>2</sub>/Al<sub>2</sub>O<sub>3</sub>/MoS<sub>2</sub> phototransistor with (e) Infrared light of 2 μm and (e) UV light (300 nm).



**Figure 3.** (a) Increase in device hysteresis with higher negative  $V_G$  sweep. Gate-tunable potentiation and conductance retention at a constant  $V_D$  of 1.0 V with the application of light of wavelengths (b) 2.0  $\mu$ m and (c) 300 nm with 512 pulses of 50 ms pulse width.

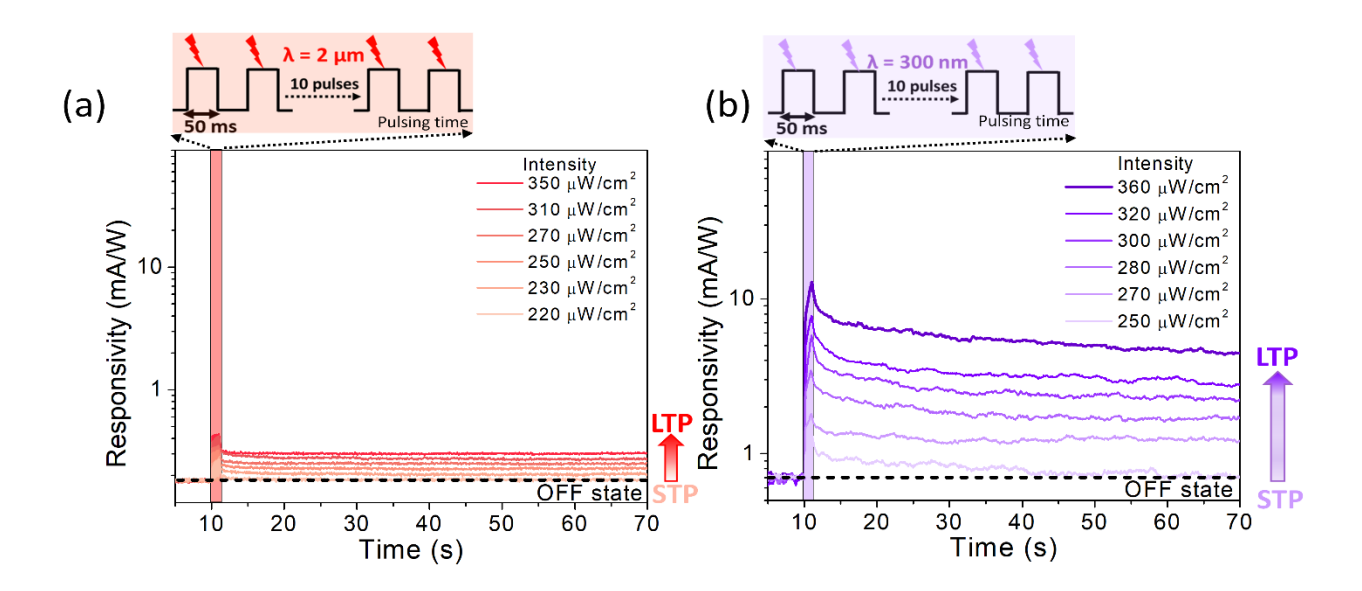


**Figure 4.** Characteristic transition of the device from short term potentiation to long term potentiation as a function of light intensity with the application of 10 light pulses of 50 ms pulse width with wavelengths (a) 2.0  $\mu$ m and (b) 300 nm at a constant  $V_G$  of -400 mV and  $V_D$  of 1.0 V.

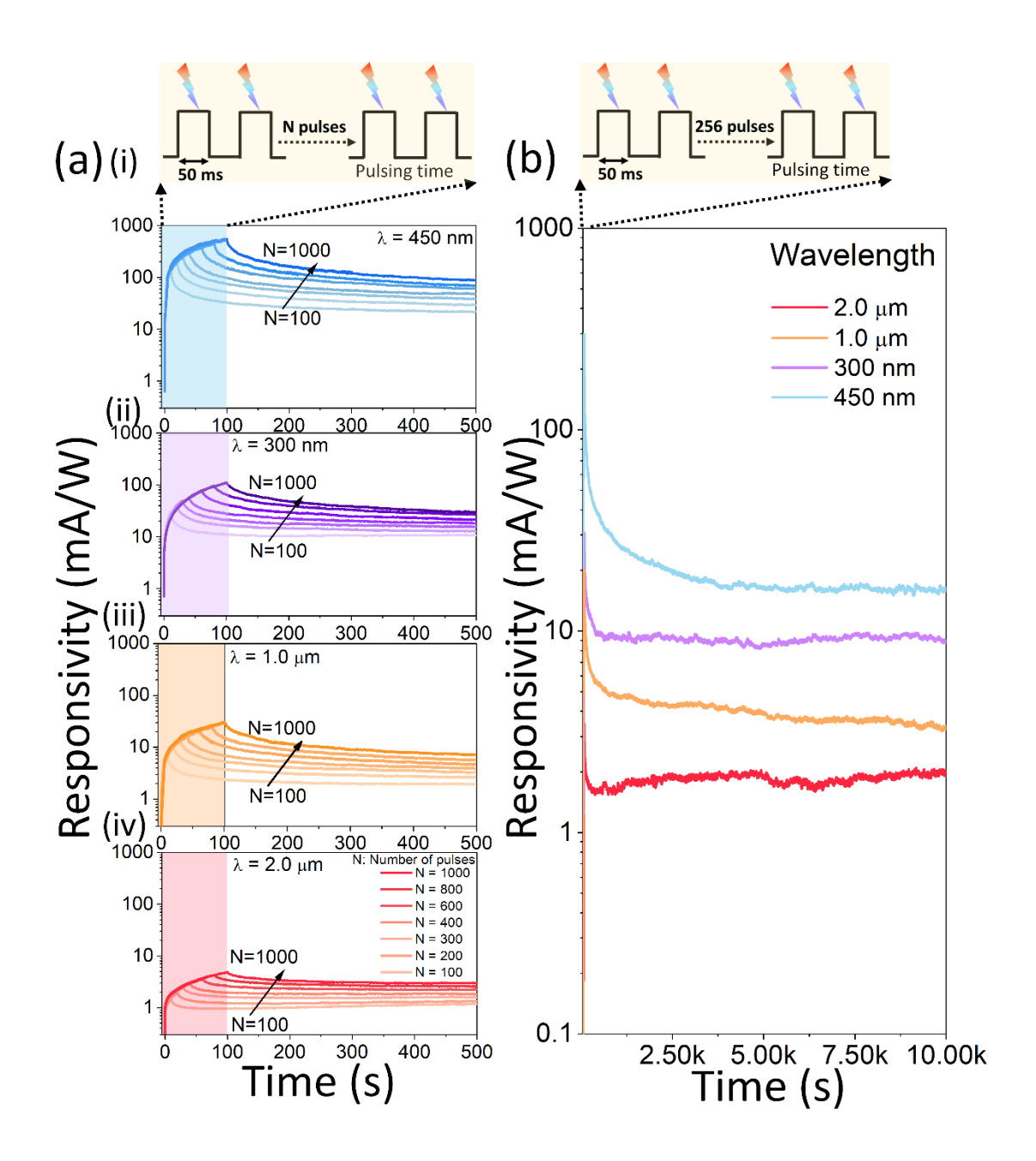


**Figure 5.** (a) Long term potentiation and memory retention with the application of light of 50 ms pulse width with wavelengths (i) 450 nm, (ii) 300 nm, (iii) 1.0 μm and (iv) 2.0 μm at a constant  $V_G$  of -400 mV and  $V_D$  of 1.0 V with increasing pulse number from 100 to 1000. (b) Retention for  $10^4$  s, after applying 256 light pulses of 50 ms pulse width with wavelengths 450 nm, 300 nm, 1.0 μm, and 2.0 μm at a constant gate bias of -400 mV and drain-source bias of 1.0 V.

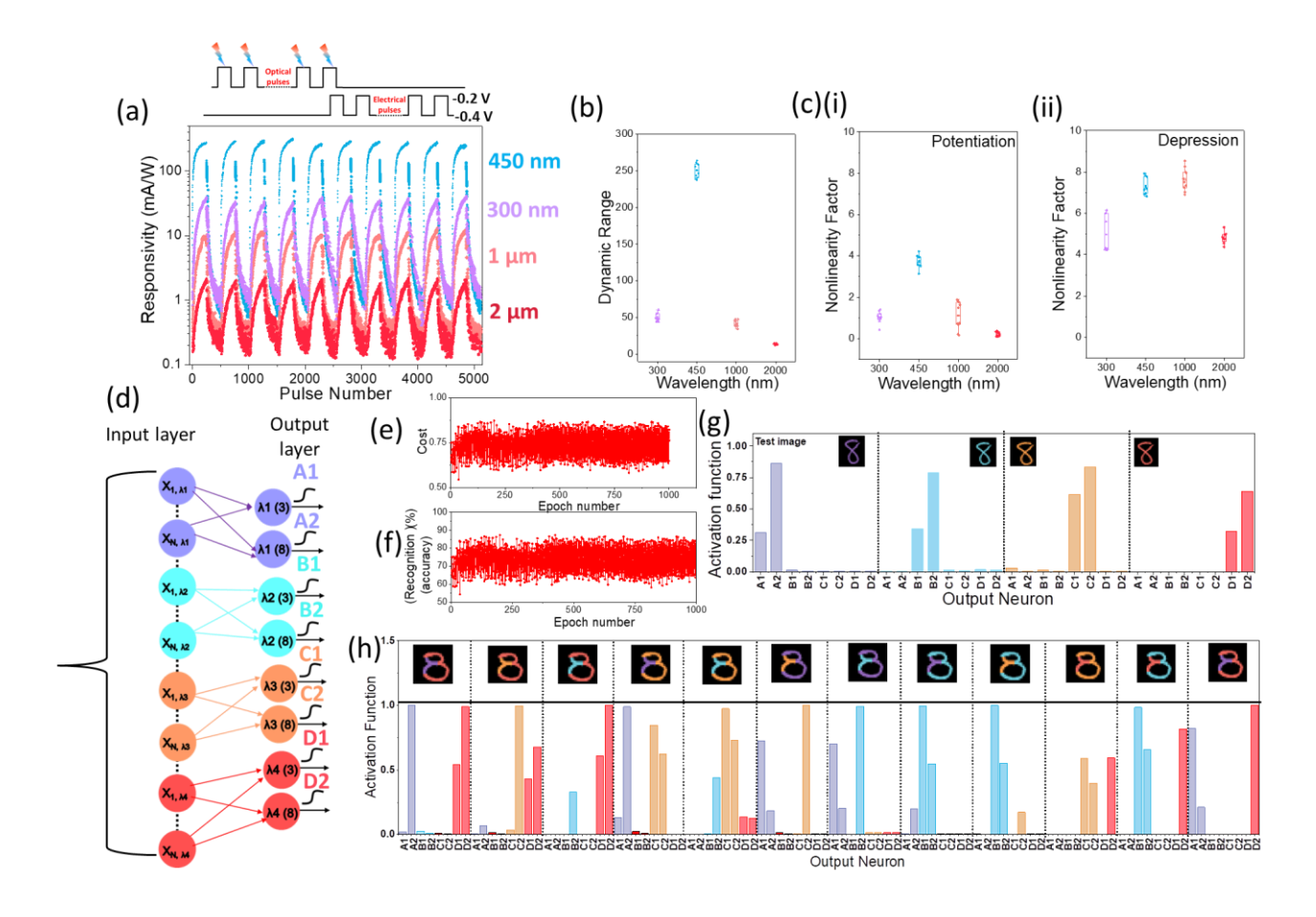


**Figure 6.** (a) Optical potentiation with 256 light pulses (50 ms ON/ 50 ms OFF) of different wavelength from 300 nm to 2.0 μm and electrical depression with 256 gate voltage pulses (30 ms ON/ 40 ms OFF) of 200 mV for 10 consecutive cycles,  $V_D = 1.0$  V was maintained throughout. (b) Dynamic range of the device at different wavelengths. (c) Nonlinearity factor calculated from the 10 cycles of (i) potentiation and (ii) depression measurements for light wavelengths of 300 nm, 450 nm, 1.0 μm and 2.0 μm. (d) Single layer neural network schematic. (e) Cost function as a function of number of training epochs for all the test cases. (f) Recognition rate as a function of number of training epochs. (g) Activation values of each neuron for single wavelength images. High activation values are observed for '3' and '8' neurons indicative of the presence of these patterns in digit '8' for 4 different wavelengths. Inset: Test image. (h). Activation values for mixed

wavelength patterns. High activation values for 3 neurons are observed corresponding to the wavelengths of inside and complement digits.

# For table of contents only

